3D density reconstruction of a screeching supersonic jet by synchronized multi-camera Background Oriented Schlieren

Lorenzo Lanzillotta[⋆] *and Olivier Léon*[⋆†] *and David Donjat*[⋆†] *and Guy Le Besnerais*[‡]
[⋆] *ONERA/DMPE, Toulouse University, France*
[‡] *ONERA/DTIS, Paris Saclay University, France*
[†]Corresponding authors: olivier.leon@onera.fr and david.donjat@onera.fr

Abstract

This work describes the application of 3D Background Oriented Schlieren (3DBOS) to the experimental analysis of the mean and instantaneous 3D structures of supersonic under-expanded screeching jets. These jets feature various dynamical states as the jet nozzle pressure ratio (NPR) is varied. Hence, six flow conditions were considered using acoustic measurements and 3D density reconstructions. Relying on the latter and on Proper Orthogonal Decomposition (POD) to isolate the main flow features, clear visualizations of the instantaneous 3D state and the reconstructed average dynamics of modes A1 and C, that are respectively axisymmetric and helical, were obtained.

1. Introduction

Supersonic axisymmetric jets are commonly found in aerospace and industrial applications, e.g. aircraft engines, space launchers or pressurized tank leakage. Such jets are often non-ideally expanded, such that the flow static pressure at the nozzle exit, p_0, is greater than the ambient one, p_a. The operating condition of these under-expanded jets is defined by the Nozzle Pressure Ratio NPR $\equiv p_{t0}/p_a$ where p_{t0} is the stagnation pressure at the nozzle exit. Equivalently, the ideally expanded Mach number can be used and is defined as

$$M_j \equiv \left(\frac{2}{\gamma - 1} \left[\mathrm{NPR}^{(\gamma-1)/\gamma} - 1 \right] \right)^{1/2} \tag{1}$$

where γ is the heat capacity ratio taken equal to 1.4. The physics of such jets is complex: in order for the flow static pressure to match the ambient one, quasi-periodic shock cell structures are generated, leading to expansion and compression waves trapped into the jet plume as illustrated by a Schlieren visualization in Fig. 1. As the NPR is increased, different regions in the jet may be identified such as Mach disks, barrel shocks or reflected shocks.

Such under-expanded jets have been extensively studied in the literature with a particular effort made toward understanding the flow field average characteristics[11] and dynamics.[10] A common feature of under-expanded jets is the presence of an aeroacoustic feedback mechanism yielding acoustic screech tones and strong flow oscillations. As initially described by Powell,[22] these tones are the result of the following feedback loop: the coherent structures associated with the jet shear-layer convective instabilities propagate downstream and interact with the shock cells, generating
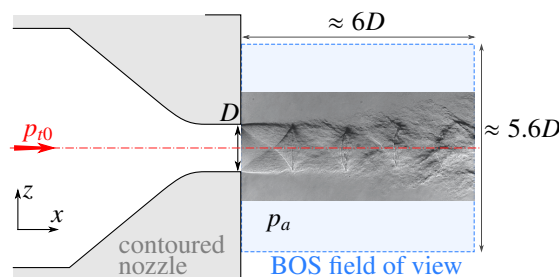
Figure 1: Schematic view of the contoured nozzle geometry studied issuing an under-expanded supersonic jet visualized using Schlieren photography; the field of view represented corresponds to the approximate one obtained with the 3DBOS setup.

upstream-propagating waves (either freestream acoustic waves or neutral upstream modes inside the jet, see Edgington-Mitchell[8] for a recent review) that, in return, excite the shear layer at the nozzle-lip, a highly receptive region. For an axisymmetric jet, four different oscillation modes were identified by Powell[22] and are commonly referred to as modes A, B, C and D. Using Schlieren visualizations and azimuthal microphone measurements, the general structure and dynamics of such jet plume global instabilities have been discussed in the literature, these four modes being generally associated with axisymmetric toroidal, rotating/precessing flapping, helical, and flapping motions respectively.

Despite decades of research effort and progress, a precise understanding of the mechanisms behind all these oscillation modes is still lacking.[8] For example, open questions remain regarding the exact nature of the screech noise production process (that is the interaction of the downstream propagating instabilities and the shock cells), the possibility of coexistence of two screech modes, or the nature of the upstream waves. Regarding the latter, recent studies conducted by Gojon et al[12] and Edgington-Mitchell et al[9] suggest for example that modes A and C can be satisfactorily modeled and explained relying on a simple vortex-sheet model where the screech feedback loop is sustained by upstream neutral acoustic wave modes, whereas the most commonly acknowledged mechanism relies on upstream near-field acoustic waves.

These questions are difficult to address because of the complexity of the different hydrodynamic and acoustic processes brought into play: hydrodynamic instabilities, shock waves disturbances, acoustic leakage and propagation, receptivity at the nozzle... each of these topics requiring deep investigations on their own. Furthermore, experimentally studying under-expanded jets to provide answers to these questions is usually challenging and studies have mainly relied on Schlieren visualizations (providing qualitative images of the flow in the form of integrated density gradients along light rays, even though quantitative information may also be retrieved[2, 15]) and on acoustic measurements[20] (giving access to only one part of the screech feedback loop). While these techniques have already led to a better understanding of the screech process over the past fifty years, it is expected that more physical insight could be obtained relying on quantitative measurements of the whole hydrodynamic field. Steps in this directions have been made using more advanced measurement techniques such as Particle Image Velocimetry (PIV)[3, 10] and Rayleigh scattering.[19]

The present work aims at going further in this direction and investigates the use of 3D Background Oriented Schlieren (3DBOS) to analyze the hydrodynamic features of the various screech modes in an under-expanded jet. Indeed, this non-intrusive measurement technique provides instantaneous and average 3D density fields, a quantity that is usually hardly accessible while being of prime importance in the study of supersonic flows.

The manuscript is organized as follows. First, descriptions of the jet facility, the 3DBOS setup, the acoustic measurements and the post-processing methodology are provided in Sec. 2. Then, near-field acoustic measurements are discussed in Sec. 3 in order to compare the properties of our screeching jet with the ones found in the literature. The first 3DBOS results are given in Sec. 4 where mean density fields are discussed. It is then detailed in Sec. 5 how phase-averaged density fields representative of the main plume instability were extracted from the 3DBOS measurements. The link between these average structures and screech noise is also discussed in this section. Finally, conclusions drawn from this preliminary work focusing on the use of 3DBOS to analyze screeching jets are given in Sec. 6.

2. Methodology

2.1 Jet facility

The jet studied was issued from a contoured convergent nozzle of exit diameter $D = 22$ mm and designed to ensure a straight sonic condition at the exit. A schematic of this nozzle is given in Fig. 1. The flow was regulated in mass-flow rate and temperature, such that the total temperature was set to $T_{t0} = 293$ K. This stagnation temperature and the Nozzle Pressure Ratio (NPR) were monitored throughout the experiment using respectively a thermocouple and a total pressure probe located 0.7 m upstream of the convergent nozzle (equivalent to $\approx 32D$).

As illustrated in Fig. 1, one particular feature of the nozzle considered in this work lies in its large lip thickness $t = 6.9$ cm $= 3.1D$. This geometry has a significant effect on the screech properties of the jet, this point being further developed in Sec. 3.

2.2 3D Background Oriented Schlieren setup

This study builds on the previous work performed by Nicolas et al,[16] with slight improvements brought to the 3DBOS setup in terms of spatial resolution. We briefly recall that the principle of BOS is to evaluate the apparent displacement of a pattern observed by a camera and induced by aero-optical effects associated with the presence of a gradient of index in-between (hot plume, compressibility effects, etc.). Pattern displacement fields and thus light ray deviation
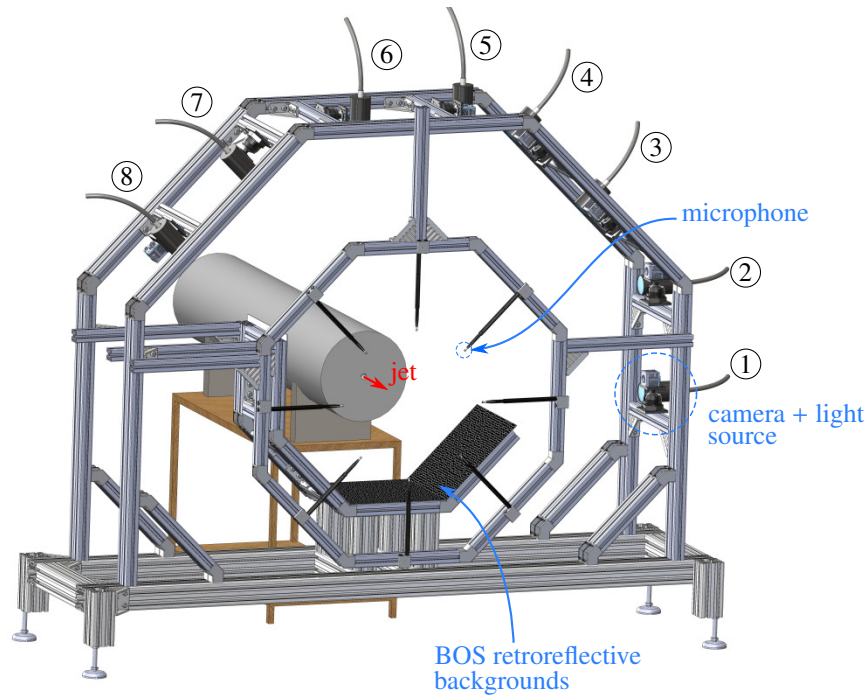
Figure 2: Schematic view of the 3DBOS setup mounted around the supersonic jet nozzle axis; the 8 cameras are placed on an arc covering an azimuthal angle of 135° and the 8 microphones are distributed on a circle every 45°.

maps obtained from a given number of point of views can then be combined to estimate the 3D density field causing these observed displacements by solving an inverse problem.

BOS images were acquired using 8 cameras (JAI BM-500GE) placed on an azimuthal arc of 1 m radius centered on the jet axis and homogeneously distributed over an azimuthal angle of 135°, as schematically shown in Fig. 2. These 5MPx cameras have a 2/3 inch sensor with a pixel size of 3.45 μm and were equipped with 50 mm focal length lenses (Schneider). With this optical setup, each camera observed an area of about 16 cm × 14 cm in a plane containing the jet axis. Four background plates were placed on the opposite side, at a distance of 0.4 m from the jet axis. The BOS backgrounds were designed using a semi-random dot pattern printed with opaque ink on a glass beads retroreflective layer. These dots had a diameter of 0.35 mm, yielding a size of 3.5 px in the images. Unlike usual printed backgrounds that exhibit Lambertian reflectance, these retroreflective backgrounds reflect the light back to its source with minimum scattering: the quantity of light reaching the camera is larger, enabling smaller apertures and thus finer spatial resolutions.

Illumination of the backgrounds was achieved using a 532 nm double-pulse laser (Quantel EverGreen 200). Only one laser pulse was used during the cameras exposure time, leading to an effective exposure time of about 10 ns, the pulse duration. This time scale ensured that the turbulent structures of the flow imaged by the cameras did not move more than about 0.1 px during each acquisition. This was regarded as sufficient in this work to consider the acquisitions as instantaneous images of the flow. Because of the high directionality of the retroreflective backgrounds reflection, each camera needed its own light source. Consequently, the laser beam was split into eight beams using a separation table made of seven 50:50 beamsplitter plates. Eight liquid guides equipped with diverging lenses were then used to direct this light toward the backgrounds. With such a setup, the amount of light collected by each camera was sufficient to operate at an optimal f-number $f_\# = 16$.[16] Under these conditions, the circle of confusion of the optical system in the region of the flow had an approximate diameter of 0.9 mm. This value is similar to the size of the interrogation window used in the post-processing algorithm (15 px) back-projected to the flow region. It is then expected that the global spatial resolution of the present BOS measurements is about 1 mm, corresponding to about $0.05D$.

The 8 cameras and the laser were synchronized using a TTL pulse generator, ensuring a synchronous observation of the flow by the cameras. During the acquisition, the camera images were transferred to the RAM of a computer and stored on a SSD disk. In order to obtain well converged first and second statistical moments of the BOS displacement fields, 6000 images were acquired for the 6 aerodynamic conditions tested, corresponding to NPR $\in \{2.1, 2.3, 2.7, 4.0, 5.0, 6.6\}$ as explained in Sec. 3. A maximum acquisition rate of 5 Hz was achieved, yielding statistically independent realizations but no relevant information about the temporal dynamics of the flow, the typical

fundamental screech frequencies measured in the present experiments ranging between 3.3 and 11.2 kHz.

2.3 3D BOS processing

3DBOS measurements first require an accurate geometrical calibration of the multicamera system. This calibration process consists in identifying all cameras internal parameters (focal length, principal points and distortion parameters) and all cameras poses (position and orientation) in the same frame of reference. To do so, we relied on the multicamera calibration methodology specifically developed for 3DBOS by Le Sant et al[14] that consists in recording several images of a 2D calibration body randomly moved inside the common field of view of all the cameras. The projection errors of all visible dots of the calibration body are then minimized through an optimization on the calibration parameters. Note that with the cameras arranged in almost half a ring as in the present work, the calibration body cannot be observed by all the cameras at once. As a consequence, the calibration process needs to handle a sequence of incomplete but overlapping views of the body to yield a global set of calibration parameters.

BOS displacement fields were then evaluated by correlating the acquired images with a reference background image that was recorded prior to the experiment. This reference image is the result of an average of 50 reference images in order to decrease the influence of the measurement noise in the correlation process of individual images. The correlation process was performed using the ONERA software FOLKI-PIV,[6] implemented on GPU (Graphic Processing Unit) and relying on an optical flow approach. Interrogation windows with a size of 15 px × 15 px were used. The deviation maps were then evaluated from the estimated displacement fields relying on the approximation that light ray deviations occur at the mid-point of the investigated volume.[5]

Using these camera calibration results and (instantaneous or average) deviation maps, 3D reconstructions of the density fields were performed. The software developed at ONERA for this purpose (MIRAGE) relies on a direct tomographic method, discussed in details by Nicolas et al,[17] aiming at inverting the equation

$$\epsilon = \frac{G}{n_{\text{ext}}} \int_{\text{ray}} \nabla \rho \; \mathrm{d}s = T(D(\rho)) = A(\rho) \,, \tag{2}$$

where ϵ is the deviation angle of a ray of light, ρ is the density, s the curvilinear coordinate along the ray and G the Gladstone–Dale constant. The observation operator A combines the tomographic operator T and the spatial derivation operator D of the density field ρ. Inverting this problem is not straightforward since A is ill-conditioned, requiring the use of a regularization method. We consider here a simple Tikhonov regularization[27] and we thus seek a minimization of a cost function $\mathcal{J}$ including a least-square data-fidelity term and a regularization function based on the density gradient such that

$$\mathcal{J}(\rho) = \|\epsilon - A(\rho)\|^2 + \lambda \|\nabla \rho\|^2 \,. \tag{3}$$

The balance between the two terms in the r.h.s. is controlled by the regularization parameter λ that was identified using a L-curve method.[13] Minimization of $\mathcal{J}$ is achieved by a conjugate gradient method. We note that other regularization methods that better account for the presence of discontinuities could have been considered, but that, overall, the present approach was observed to yield shock waves that are not excessively smoothed. Nonetheless, future work may consider the use of other regularization methods to improve the sharpness of the solution.

A 3D mask in the form of a truncated cone diverging downstream was designed to reduce the number of voxels considered in the reconstruction process and to limit the diffusion of the information out of the region of interest. The use of such a mask additionally helps to reduce the computational cost.[5, 17] Free boundary conditions were imposed on both inlet and outlet boundaries to account for the jet flow, while a (constant) external density, measured during the experiment, was enforced on the remaining lateral boundary of the 3D mask. Finally, we note that the code is implemented on a GPU architecture to reduce the computation time and to allow the reconstruction of large fields. Here the reconstruction volume was about 13 cm × 6.5 cm × 6.5 cm and made of about 4.5×10^6 square voxels having a size of 0.5 mm.

2.4 Acoustic measurement setup

The temporal dynamics of the jet flow was indirectly scrutinized through acoustic measurements. This was performed using 1/4 inch microphones (GRAS 46DB) having a dynamic range upper limit of 166 dB and a frequency range of 70 kHz. Two microphone setups were considered. In the first configuration, four microphones were mounted along an arc of radius $r = 20D$, centered on the jet axis at $x = 1D$ and with polar angles measured from downstream $\theta = 30°$, $50°$, $70°$ and $90°$. This setup allowed studying the jet noise directivity and was employed to analyze the screech properties of the jet presented in the following Sec. 3. In the second setup that is schematically represented in Fig. 2,
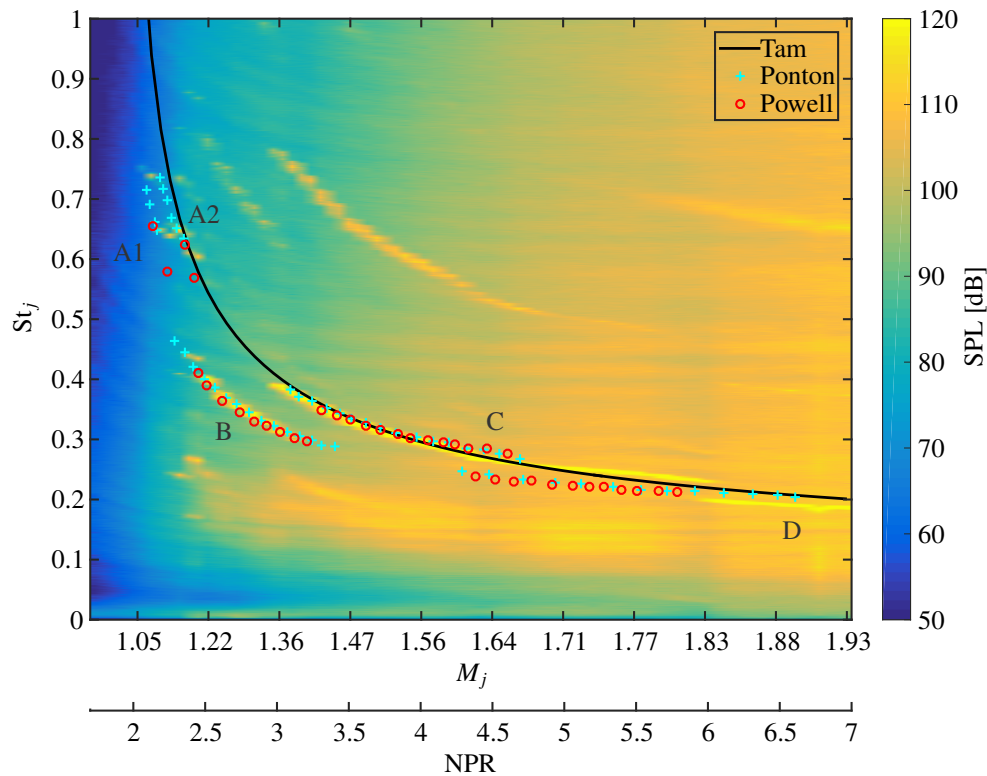
Figure 3: Contours of sound pressure level (SPL) as function of jet operating conditions (NPR and Mach number M_j). The solid black line is the semi-empirical relation proposed by Tam,[26] the blue and the red dots are representative of measurements obtained by Ponton and Seiner[21] and Powell[22] respectively.

eight microphones were evenly mounted (every 45°) on a ring centered on the jet axis in order to analyze the azimuthal distribution of the jet acoustic field. This ring was positioned at $x = 21D$ and the microphones were located at $r = 13D$.

These acoustic measurements were not performed in anechoic conditions, but care was taken to attenuate the acoustic reflections on the floor and the walls of the facility as well as on the BOS structure itself using acoustic foam panels. These muffled conditions were observed to be sufficient for the present analysis. Indeed, very limited reflection artifacts were observed on the acoustic spectra. Furthermore, it should be noted that this work is primarily focusing on the analysis of the jet screech effects that occur at very specific frequencies and with large sound pressure levels that easily emerge from the background noise. Finally, it was verified that the presence of the 3DBOS bench did not modify the frequencies and the levels of the screech noise measured, ensuring the relative non-intrusivity of our setup and measurement technique.

3. Screech properties of the jet studied

Preliminary acoustic measurements were performed to characterize the jet screech frequencies obtained with this setup. As mentioned in Sec. 2.1, the jet studied is issuing from a nozzle designed with a very thick lip, a geometrical feature that needs to be considered when comparing the present results with the literature. Indeed, it was shown in previous works that the lip thickness is an important parameter in the overall screech feedback process. More precisely, Ponton and Seiner[21] and Shen and Tam[24] observed a delayed screech cessation (in terms of NPR or M_j values) as the lip thickness was increased, together with a significant increase in screech noise levels (also reported by Norum[18] and Raman[23]). Furthermore, nozzle lip thickness was reported to induce slight shifts in screech frequencies by Aoki et al.[4] Finally, this geometrical parameter was observed to play a determinant role in the transition between screech modes:[7,21] first, in thick-lip configurations, an earlier transition in terms of NPR between modes B and C was reported compared to thin-lip cases; second, the range of NPR over which intermittent switching between these two modes occurs was observed to be reduced; third, mode C was observed to extend over a larger range of NPR values, meaning that the transition to mode D should occur at larger NPR values compared to thin-lip cases.

Fig. 3 was obtained using the first acoustic measurement setup presented in Sec. 2.4 using only the most downstream microphone (at $\theta = 30°$ from the jet axis). This figure provides contours of Sound Pressure Level (SPL) as a

function of the NPR (or equivalently M_j using Eq. (1)) and the Strouhal number $\mathrm{St}_j \equiv f D_j / U_j$ where f is the frequency, D_j the fully expanded diameter and U_j the fully expanded jet velocity. Screech tones are observed in this figure as thin spectral bands of large SPL decreasing as the NPR increases. The main modes reported in the literature are labeled next to the fundamental spectral bands while the first harmonics are left aside. Together with these acoustic measurements are plotted some classical results reported in the literature. The solid black line corresponds to the semi-empirical law proposed by Tam et al[26] that reads

$$\mathrm{St}_j = 0.67(M_j^2 - 1)^{-1/2} \left[1 + 0.7 M_j \left(1 + \frac{\gamma - 1}{2} M_j^2 \right)^{-1/2} \left(\frac{T_a}{T_{t0}} \right)^{-1/2} \right]^{-1} , \tag{4}$$

where T_a / T_{t0} is the ratio of the ambient to the total temperature of the jet. As one can observe, this smooth function provides overall satisfactory estimates of the screech frequencies for modes A, C and D. Note however, that, by design, it cannot account for the modes staging phenomenon and for the frequencies of mode B. In addition to this curve, experimental results obtained by Powell[22] and Ponton and Seiner[21] for thinner lip configurations are superposed. A satisfactory agreement in obtained for NPR values lower than 4. For NPR > 5, in agreement with the literature mentioned previously, the mode C from our thick-lip screeching jet extends over a larger range, up to NPR = 6.1. In addition, no screech cessation was observed up to the maximum NPR = 7 reached.

Based on these results, six values of NPR were selected to further investigate the different screeching modes using 3DBOS: 2.1 (mode A1), 2.3 (mode A2), 2.7 (mode B), 4.0 and 5.0 (mode C) and 6.6 (mode D). These values were chosen to lie in the middle of each mode spectral band in order to ensure stable conditions and avoid at best modes intermittency and switching.

4. Mean density fields results

This section details the properties of the 3D mean density fields obtained by 3DBOS for the six NPR conditions identified in Sec. 3 using acoustic measurements. The results are gathered in Fig. 4, displaying 3D density iso-surfaces and density contours in a longitudinal plane. Examining the 3D iso-surface plots, axisymmetric mean density fields are well recovered for all the conditions, which is to be expected. Shock cells appear to be furthermore well captured and one can clearly visualize the increase of the spacing between the cells as the NPR is increased. These shock cells are more readily observed in the density contours extracted from the $y = 0$ plane, which also illustrate the presence of Mach disks for the last three NPR conditions.

In order to compare the mean properties of the present jet with the ones reported in the literature, quantitative data regarding the topology of these jets were extracted from these 3DBOS reconstructions. First, the mean shock spacing L_s was evaluated for each NPR. These results are compared in Fig. 5a with the Prandtl-Pack formula that reads

$$\frac{L_s}{D} = 1.306(M_j^2 - 1)^{1/2} . \tag{5}$$

A satisfactory agreement is observed, displaying an increase of the shock spacing for increasing values of the NPR.

Second, the average diameter of the first Mach disk D_{MD} appearing for a NPR ≈ 4 was evaluated based on the gradient amplitude of the reconstructed density fields for the three highest NPRs studied. These results are compared in Fig. 5b with experimental results reported by Nicolas et al[16] and by Addy[1] for a contoured nozzle similar to the one here studied. Furthermore, estimates of D_{MD} were also extracted from Schlieren visualizations performed under similar conditions and from a RANS simulation performed by the authors. The overall agreement with all the results is satisfactory, especially with Addy's, suggesting that the present facility and jet main characteristics do not feature significant geometrical or aerodynamic imperfections. We finally note that the main source of uncertainty in the estimation of D_{MD} from our 3D density results is expected to lie in the spatial resolution of the technique. This uncertainty remains nonetheless sufficiently low to have confidence in the accuracy of the spatial features of the flow evidenced by the 3DBOS technique. Particularly, one can observe an improvement on the estimation of D_{MD} compared to the previous 3DBOS setup used by Nicolas et al[16] at NPR = 5.

5. 3D density fields of screech modes

The low acquisition rate of the 3DBOS system prevents us from performing a spatio-temporal analysis of the jet dynamics associated with screech. Nonetheless, the absolute instability at the root of screech is expected to significantly alter the jet density field in the form of large coherent oscillations in the jet plume: its coherent imprints should be observed on the instantaneous BOS displacement fields obtained from each camera, as shown in Sec. 5.2. Following the work of Nicolas et al,[16] we thus propose to rely on a Proper Orthogonal Decomposition (POD) of the displacement

(a) NPR = 2.1

(b) NPR = 2.3

(c) NPR = 2.7

(d) NPR = 4.0

(e) NPR = 5.0

(f) NPR = 6.6
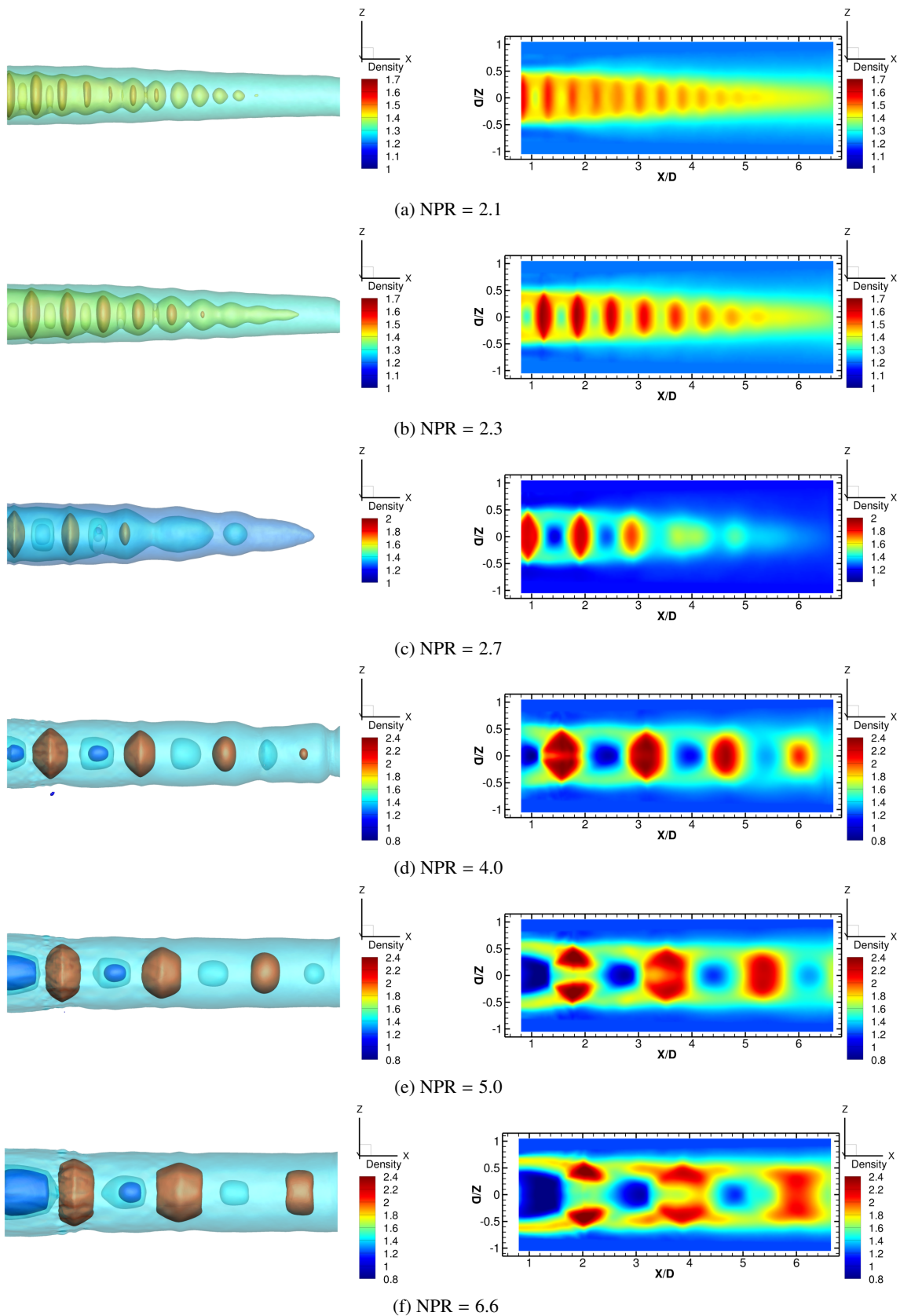
Figure 4: Mean 3DBOS results obtained for the six NPR selected; left column: 3D iso-surfaces of mean density; right column: contours of mean density in the plane $y = 0$.
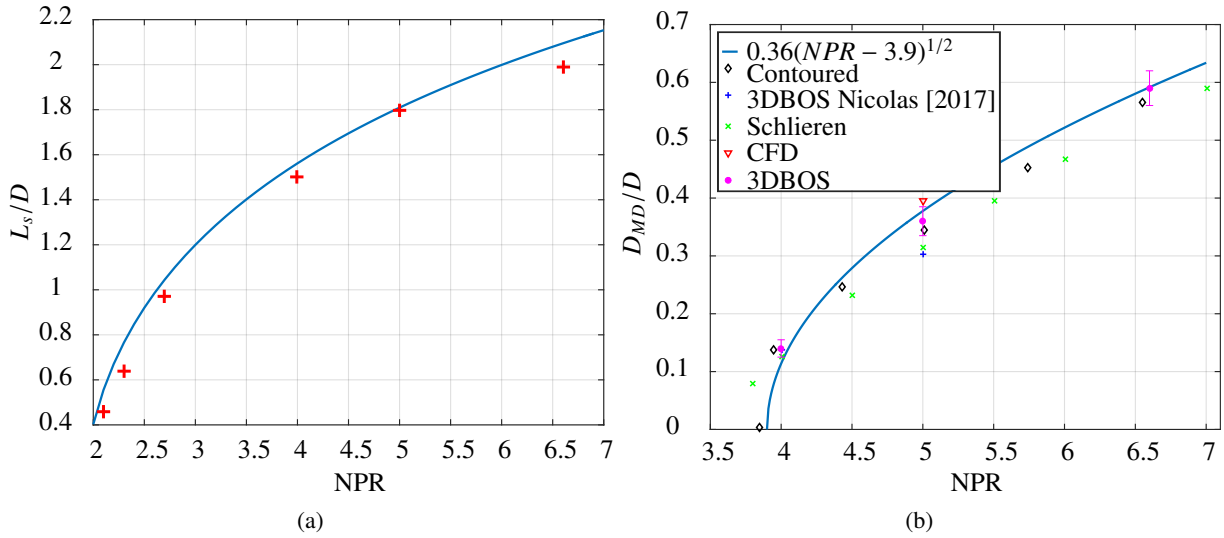
Figure 5: (a) Mean shock spacing L_s/D as a function of jet operating conditions: the solid line is the Prandtl-Pack formula (Eq. (5)) and red plus markers correspond to the present mean 3DBOS results; (b) First Mach disk diameter D_{MD}/D as a function of the jet NPR: the blue solid line is the relation proposed by Addy;[1] the black diamonds are experimental data from Addy;[1] the blue plus markers were obtained from 3DBOS by Nicolas et al;[16] the green crosses correspond to Schlieren visualizations; the red inverted triangle is from RANS simulation; the magenta dots correspond to the results of the present experiment. Note that the last four data sets were obtained with the same jet facility.

fields (and not the 3DBOS instantaneous density fields for a computational cost reason) in an attempt to isolate the main coherent features associated with the plume instability. A similar approach was also considered by Edgington-Mitchell et al[10] to study the dynamics of the screech mode C relying on PIV data.

In the present work, the displacement field d obtained with only one camera among the eight available was considered since it was observed to provide sufficiently reliable data for this first investigation. A consequence of this choice is that complex screech dynamics such as flapping were not satisfactorily captured (that is for modes B and D), and only axisymmetric and purely helical features (modes A and C) were observed to be efficiently isolated. Hence, only these two last modes A and C (that is the two cases where NPR equals 2.1 and 4.0) are further analyzed in this section. Future work will however consider the use of all the cameras to thoroughly isolate the dominant structures at all the screech modes. Note that the choice of the camera considered for the following analysis does not modify the results: each camera having a similar point of view on the jet by rotational symmetry around the jet axis, similar decompositions will be obtained.

5.1 Proper Orthogonal Decomposition results

POD is performed using the Snapshot POD method proposed by Sirovich[25] since the number of images acquired per camera ($N = 6000$) is much lower than the number of displacement vectors evaluated per image (typically around 20 000). We briefly recall that this approach seeks a decomposition of the displacement fluctuation field $d'(x, t_j)$ in the form of orthonormal spatial modes ϕ_i that optimally capture the variance of the data. We have

$$d'(x, t_j) = \sum_{i=1}^{N} a_i(t_j)\phi_i(x) \tag{6}$$

where $a_i(t_j)$ are random variables of the time t_j. Note that since the present experiment is not time-resolved, these a_i coefficients are functions of the discrete time variable t_j and do not represent the temporal dynamics of the modes. These spatial modes ϕ_i and expansion coefficients a_i are obtained following this classical procedure: first, the (temporal) correlation matrix R associated with the displacement vectors d' is evaluated using the L^2 inner product; second, an eigenvalue decomposition of R provides "temporal" modes a_i and eigenvalues λ_i that represent the energy content of each mode (usually sorted in descending order); finally, spatial POD modes are retrieved by the projection

$$\phi_i(x) = \frac{1}{N\lambda_i} \sum_{j=1}^{N} a_i(t_j)d'(x, t_j). \tag{7}$$

8
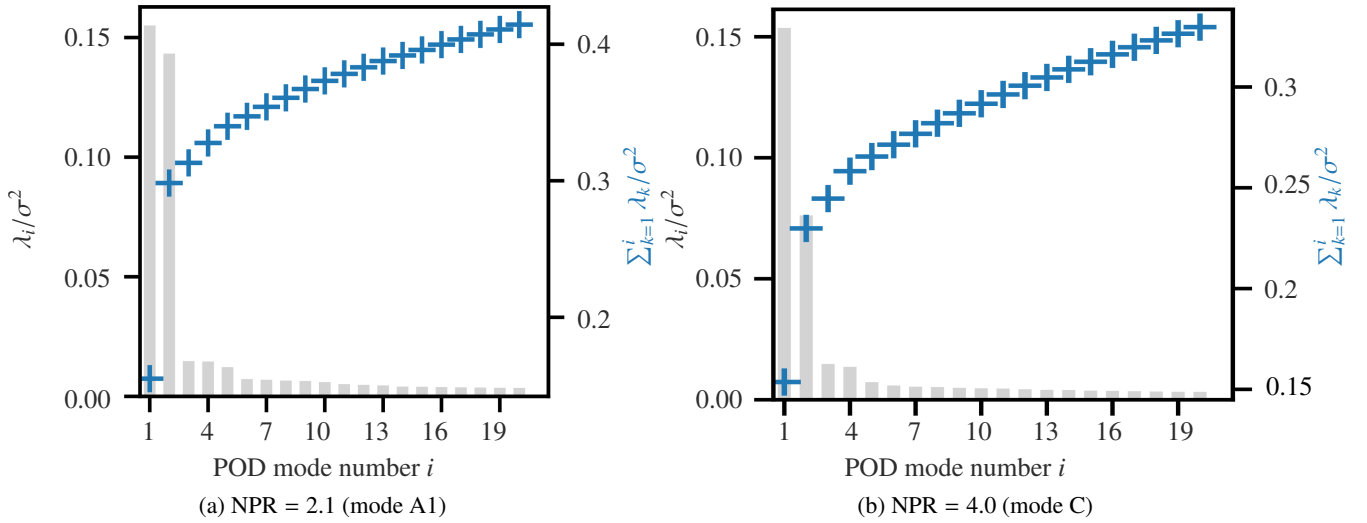
Figure 6: Normalized POD eigenvalues λ_i/σ^2 obtained on the BOS displacement fields of one camera for two NPR values. These eigenvalues are made dimensionless using the total displacement variance σ^2. The cumulative sum of these eigenvalues (right vertical axis) indicates the fraction of energy captured with an increasing number of modes.

Applying this approach to the displacement fields obtained for the two NPRs 2.1 and 4.0 yielded the distribution of eigenvalues λ_i given in Fig. 6. One can clearly observe the emergence of the first two eigenvalues in both cases. For the first case (NPR = 2.1), they contribute to about 30% of the total variance, while for the second case (NPR = 4.0) to about 25%. This observation suggests that we may rely on such two modes to analyze the main coherent organization of the flow in both cases. It appears however for now very uncertain to claim here that they are exactly representative of the spatio-temporal dynamics of screech modes. This point will be further discussed in Sec. 5.3.

The spatial POD modes $\boldsymbol{\phi}_i = (\phi_i^{(x)}, \phi_i^{(z)})^T$ associated with these first two eigenvalues for the two NPR cases are displayed in Fig. 7, showing both the horizontal (along x) and vertical (along z) displacement components. Examining these spatial POD modes, it can be observed that for the two aerodynamic conditions, the first two modes selected display a similar spatial structure, with comparable spatial axial wavelength (shifted streamwise by about a quarter-wavelength between the two modes). For the case NPR = 2.1, we observe a wave-packet-like perturbation that is symmetric along the axis x for the axial component and anti-symmetric for the vertical component. Such a structure is reminiscent of what would be obtained with a Kelvin-Helmholtz-type instability.[9] For the second case NPR = 4.0 we observe that the two spatial modes still display a wave-packet-like structure outside of the jet (that might be the imprint of screech noise radiation) but with also a significant contribution of fluctuations from the shock cells inside the jet. The symmetry along the axis x is different compared to the case NPR = 2.1: the axial component of displacement is anti-symmetric along x while the vertical component is symmetric. Such a structure is reminiscent of what would be obtained with an helical instability with unit azimuthal wavenumber.[10] These observations are thus consistent with the general physical behavior of screech modes reported in the literature for the modes A and C here studied.

The previous observation that the first two dominant POD modes of each NPR case have similar structures suggests that they could be coupled and representative of a similar convective and oscillatory feature like the global instability associated with screech. One way to investigate such a coupling is to plot the state of each BOS acquisition in the subspace generated by the two dominant modes $(\boldsymbol{\phi}_1, \boldsymbol{\phi}_2)$, yielding the scatter plot $(a_1(t_j), a_2(t_j))$. If the measurements were temporally resolved, this would lead to a Lissajous figure (or a phase-portrait in terms of dynamic systems) and a purely oscillating dynamics would generate a circle in such a phase-space. The results for the two NPR values considered are displayed in Fig. 8. One can clearly observe that both scatter plots statistically draw a circle with some radial dispersion, supporting a phase-coupling between the two modes that are thus likely representative (statistically) of a convective oscillatory dynamics linked to the plume instability. Further support on this point will be provided in Sec. 5.3.

The plots given in Fig. 8 finally offer a way to sort all the BOS images obtained with all the cameras: dividing the two plots in twelve angular sectors, we can define for each BOS acquisition a given "phase" relative to the first two dominant POD modes identified with one camera. This procedure is illustrated in this figure by filling the markers with 12 different colors. Evaluating the associated phase-average of the displacement fields for each camera based on this sorting procedure yields 12 mean displacement fields for each camera and finally 12 phase-averaged 3D density fields after reconstruction. These 3D results are displayed in Fig. 9. As one can observe, relying on this methodology leads

(a) NPR = 2.1

(b) NPR = 4.0
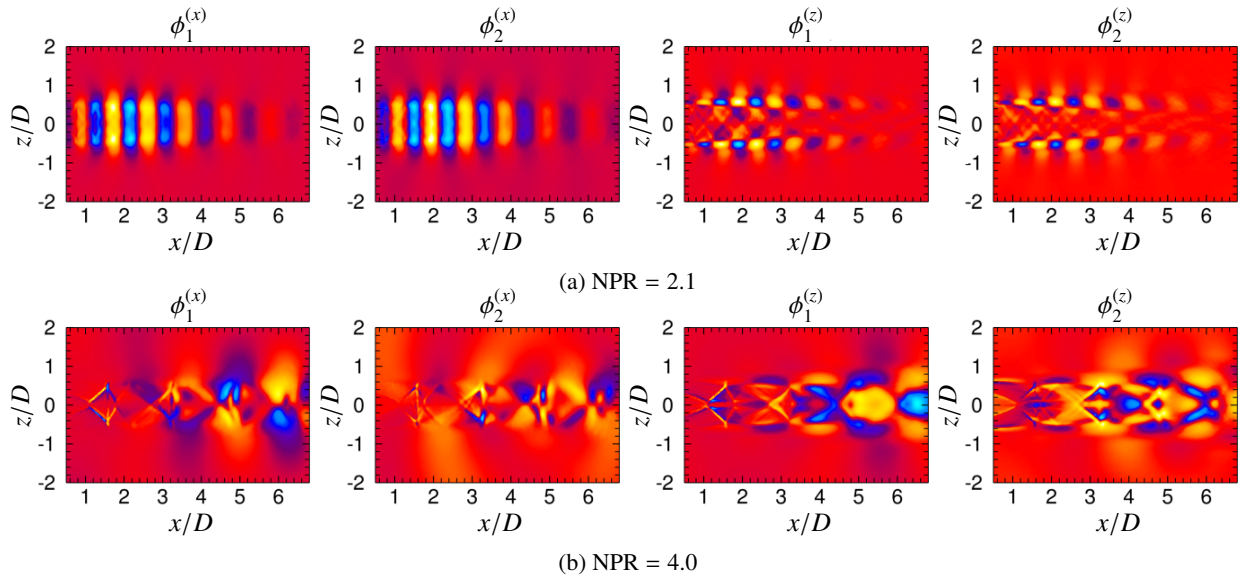
Figure 7: Axial ($\phi_i^{(x)}$) and vertical ($\phi_i^{(z)}$) components of the first two POD spatial modes ($i \in [1..2]$) obtained by considering the BOS displacement fields of one camera for 2 values of NPR.

to phase-averaged 3D density fields that are axisymmetric for NPR = 2.1 and helical for NPR = 4.0. These results are in line with the accepted topology of the plume instabilities associated with screech modes A1 and C. This is however the first time to the knowledge of the authors that such average 3D structures are actually reconstructed, assuming that the present methodology provides a representative image of the instabilities associated with screech.

We conclude this section by noting that these phase-averaged reconstructed density fields allow us to qualitatively observe the phase-averaged dynamics of the shock cells for the two NPRs considered. For NPR = 2.1 (mode A1), the first shock cells appear to be significantly disturbed by the perturbation, with forward and backward oscillations. For NPR = 4.0 (mode C), it is observed that the second, third and fourth shock cells remain at the same axial locations but appear to sustain a precession around the x axis, moving in a circular motion within a plane that tilts slightly and periodically with respect to the (yz) plane.

5.2 Instantaneous 3D density fields

To highlight the fact that 3D structures identified by the previous methodology relying on POD does not provide completely artificial results, Fig. 10 provides instantaneous 3D density reconstructions obtained for the case NPR = 4.0. These four instantaneous fields were arbitrarily chosen from the data shown in the scatter plot of Fig. 8b in the angular sectors corresponding to $\psi = 0°$, $90°$, $180°$ and $270°$. While these reconstructions do not provide as smooth density fields as the phase-averaged results, a similar helical organization of the flow can clearly be observed, confirming the physical relevance of the 3D structures previously identified.

5.3 On the link between POD results and screech modes

Finally, a central question that one may ask is whether the 3D coherent structures previously identified using (spatial-only) POD are relevant in the description of the (spatio-temporal) screech modes or not. To investigate the possible connection between POD modes and screech noise, 3DBOS measurements were performed together with acoustic measurements using the second acoustic setup presented in Sec. 2.4, that is with an azimuthal array of microphones shown in Fig. 2. For each BOS acquisition, an oscilloscope acquired the laser Q-switch signal, defining the exact time at which BOS images were recorded, and the acoustic signal of six microphones over at least ten acoustic periods associated with the screech frequency. These acoustic measurements were then post-processed using a narrow digital 100 Hz band-pass filter centered on the screech frequency (with zero phase-shift) and a Hilbert transform to provide a phase estimate of each BOS acquisition with respect to screech. Note that in this process, one actually needs to account for the phase-shift induced by the location of the microphones with respect to the source of screech noise, a distance that is not precise and likely stochastically fluctuates due to the motion of the shock waves.

To illustrate the results obtained following this approach, let us consider the case NPR = 4.0. Similarly to what was performed with POD, BOS acquisitions were divided into 12 "screech phase" classes. An easy way to visualize the

(a) NPR = 2.1

(b) NPR = 4.0
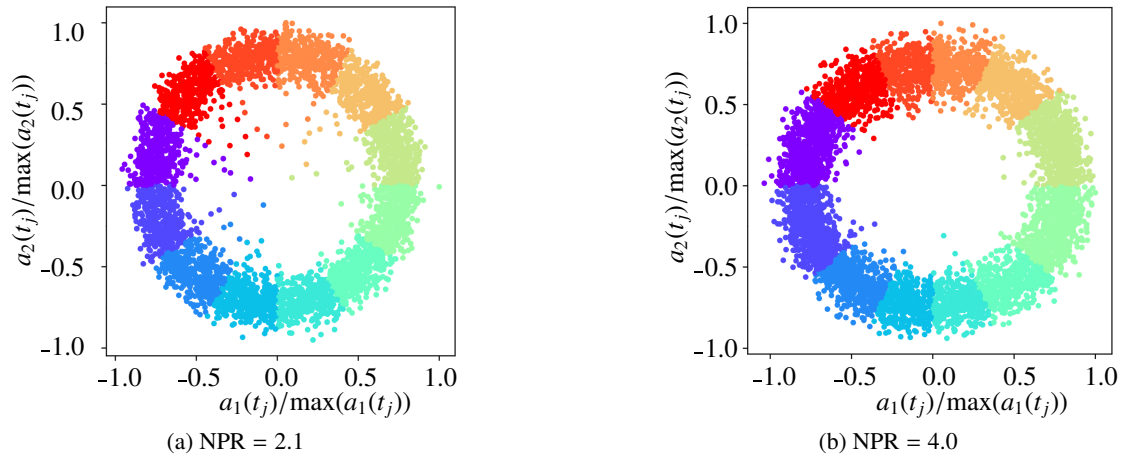
Figure 8: Scatter plots $(a_1(t_j), a_2(t_j))$ giving the state of all BOS acquisitions (of one camera, $j \in [1..N]$) in the subspace generated by the first two POD spatial modes $\phi_i(x)_{i \in [1..2]}$ for the two NPR conditions corresponding to screech modes A1 and C. Colors highlight the division of the scatter plot to define 12 phase classes.

(a) NPR = 2.1

(b) NPR = 4.0
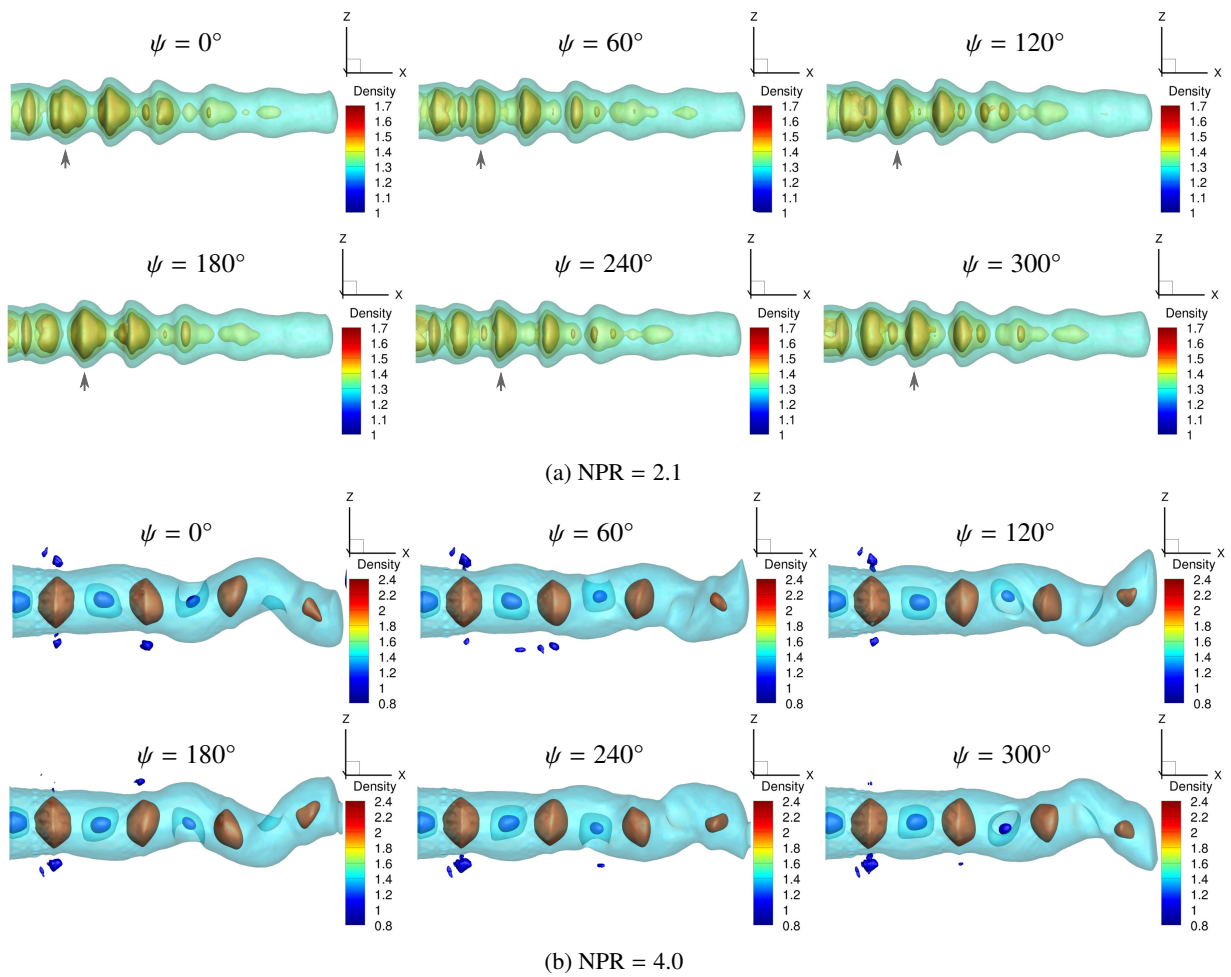
Figure 9: Phase-averaged 3D density fields obtained by 3DBOS using the first two spatial-POD modes to sort the images of the 8 cameras for the two NPR conditions corresponding to the screech modes A1 and C.

3DBOS OF A SCREECHING SUPERSONIC JET
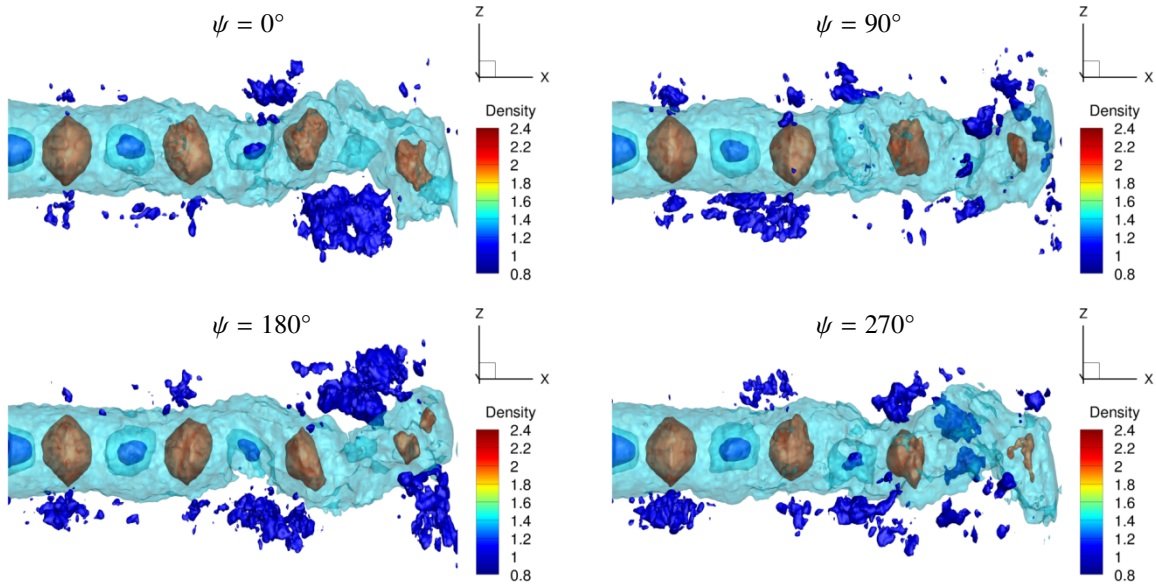
Figure 10: Iso-surfaces of 4 instantaneous 3D density fields reconstructed by 3DBOS for the case NPR = 4.0; the phase ψ of these fields was evaluated relatively to the first two spatial POD modes.

results in comparison with the ones obtained by POD is to consider the scatter plot of POD coefficients in Fig. 8b and to set the colors of the markers as a function of the "screech phase" here evaluated. If the two approaches were equivalent, the colored version of Fig. 8b would be exactly retrieved. The plot obtained is shown in Fig. 11: a dispersion of the markers of similar color can be observed, suggesting that some differences exist. Nonetheless, one can notice that this dispersion is not uniform, but that it is centered around each phase class considered, over an angle of about 90°. This Fig. 11 appears as a dispersed version of Fig. 8b maintaining the overall phase class order previously identified. We thus suggest that, while the details of the two approaches are different, they capture on average the same physics. In other words, we believe that these results support the idea that the POD analysis performed previously is actually relevant in isolating the average modes associated with screech noise. The dispersion observed in the present results is likely the consequence of either some jittering of the screech modes (we observed for example slight variations of its frequency over a complete acquisition sequence) or some spatial fluctuation of the source of screech with respect to the microphone locations; an other possible origin may be the uncertainty in the phase estimation process using the Hilbert transform.

6. Conclusion

In this work, the non-intrusive, seedless 3DBOS technique was applied to measure the 3D density fields of under-expanded screeching jets. Compared to the previous work of Nicolas et al,[16] a significant improvement on the spatial resolution of the technique was achieved using retro-reflective backgrounds, yielding smaller lens apertures and reduced astigmatism effects. As a consequence, satisfactory mean and instantaneous 3D density reconstructions were obtained, enabling a future deeper analysis of the structure of the 3D shock cells and their impact on the downstream instabilities associated with screech. Furthermore, it was shown that the fluctuating density field associated with the main (average) instability wave driving screech for modes A1 and C could be satisfactorily isolated from the BOS measurements relying on the first two POD modes of the BOS displacement fields. The relevance of these isolated coherent structures in the description of the screech process was evidenced using acoustic measurements. A clear 3D visualization of the two modes A1 and C was obtained, displaying axisymmetric and helical structures. The other modes proved more difficult to analyze following this methodology and future work will address this point.

Acknowledgments
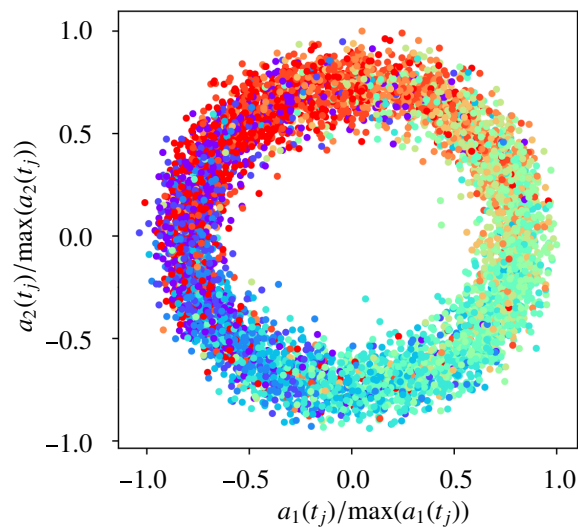
Figure 11: Scatter plot similar to Fig. 8b, but with marker colored by the phase value determined by acoustic measurements.

References

[1] A. L. Addy. Effects of axisymmetric sonic nozzle geometry on mach disk characteristics. *AIAA Journal*, 19(1):121–122, January 1981.

[2] Benoît André, Thomas Castelain, and Christophe Bailly. Shock-tracking procedure for studying screech-induced oscillations. *AIAA Journal*, 49(7):1563–1566, July 2011.

[3] Benoît André, Thomas Castelain, and Christophe Bailly. Investigation of the mixing layer of underexpanded supersonic jets by particle image velocimetry. *International Journal of Heat and Fluid Flow*, 50:188–200, December 2014.

[4] Toshiyuki Aoki, Yong-Hun Kweon, Yoshiaki Miyazato, Heuy-Dong Kim, and Toshiaki Setoguchi. An experimental study of the nozzle lip thickness effect on supersonic jet screech tones. *Journal of Mechanical Science and Technology*, 20(4):522–532, April 2006.

[5] Bradley Atcheson, Ivo Ihrke, Wolfgang Heidrich, Art Tevs, Derek Bradley, Marcus Magnor, and Hans-Peter Seidel. Time-resolved 3d capture of non-stationary gas flows. In *ACM transactions on graphics (TOG)*, volume 27, page 132. ACM, 2008.

[6] F. Champagnat, A. Plyer, G. Le Besnerais, B. Leclaire, S. Davoust, and Y. Le Sant. Fast and accurate PIV computation using highly parallel iterative correlation maximization. *Experiments in Fluids*, 50(4):1169–1182, March 2011.

[7] Thiago Lima de Assunção. *Experimental study of underexpanded round jets: nozzle lip thickness effects and screech closure mechanisms investigation*. PhD thesis, Université de Poitiers, 2018.

[8] Daniel Edgington-Mitchell. Aeroacoustic resonance and self-excitation in screeching and impinging supersonic jets – a review. *International Journal of Aeroacoustics*, 18(2-3):118–188, March 2019.

[9] Daniel Edgington-Mitchell, Vincent Jaunet, Peter Jordan, Aaron Towne, Julio Soria, and Damon Honnery. Upstream-travelling acoustic jet modes as a closure mechanism for screech. *Journal of Fluid Mechanics*, 855, September 2018.

[10] Daniel Edgington-Mitchell, Kilian Oberleithner, Damon R. Honnery, and Julio Soria. Coherent structure and sound production in the helical mode of a screeching axisymmetric jet. *Journal of Fluid Mechanics*, 748:822–847, May 2014.

[11] Erwin Franquet, Vincent Perrier, Stéphane Gibout, and Pascal Bruel. Free underexpanded jets in a quiescent medium: A review. *Progress in Aerospace Sciences*, 77:25–53, August 2015.

[12] Romain Gojon, Christophe Bogey, and Mihai Mihaescu. Oscillation modes in screeching jets. *AIAA Journal*, 56(7):2918–2924, July 2018.

[13] Per Christian Hansen. Analysis of discrete ill-posed problems by means of the l-curve. *SIAM Review*, 34(4):561–580, December 1992.

[14] Yves Le Sant, Violaine Todoroff, Anthelme Bernard-Brunel, Guy Le Besnerais, Francis Micheli, and David Donjat. Multi-camera calibration for 3dbos. In *17th international symposium on applications of laser techniques to fluid mechanics*, 2014.

[15] Bertrand Mercier, Thomas Castelain, and Christophe Bailly. Experimental characterisation of the screech feedback loop in underexpanded round jets. *Journal of Fluid Mechanics*, 824:202–229, July 2017.

[16] F. Nicolas, D. Donjat, O. Léon, G. Le Besnerais, F. Champagnat, and F. Micheli. 3d reconstruction of a compressible flow by synchronized multi-camera BOS. *Experiments in Fluids*, 58(5), April 2017.

[17] F. Nicolas, V. Todoroff, A. Plyer, G. Le Besnerais, D. Donjat, F. Micheli, F. Champagnat, P. Cornic, and Y. Le Sant. A direct approach for instantaneous 3d density field reconstruction from background-oriented schlieren (BOS) measurements. *Experiments in Fluids*, 57(1), December 2015.

[18] T. D. Norum. Screech suppression in supersonic jets. *AIAA Journal*, 21(2):235–240, February 1983.

[19] J. Panda and R. G. Seasholtz. Measurement of shock structure and shock–vortex interaction in underexpanded jets using rayleigh scattering. *Physics of Fluids*, 11(12):3761–3777, December 1999.

[20] Michael K. Ponton and John M. Seiner. Acoustic study of b helical mode for choked axisymmetric nozzle. *AIAA Journal*, 33(3):413–420, March 1995.

[21] M.K. Ponton and J.M. Seiner. The effects of nozzle exit lip thickness on plume resonance. *Journal of Sound and Vibration*, 154(3):531–549, May 1992.

[22] A Powell. On the mechanism of choked jet noise. *Proceedings of the Physical Society. Section B*, 66(12):1039–1056, December 1953.

[23] Ganesh Raman. Cessation of screech in underexpanded jets. *Journal of Fluid Mechanics*, 336:69–90, April 1997.

[24] Hao Shen and Christopher K. W. Tam. Effects of jet temperature and nozzle-lip thickness on screech tones. *AIAA Journal*, 38(5):762–767, May 2000.

[25] Lawrence Sirovich. Turbulence and the dynamics of coherent structures. i. coherent structures. *Quarterly of applied mathematics*, 45(3):561–571, 1987.

[26] C.K.W. Tam, J.M. Seiner, and J.C. Yu. Proposed relationship between broadband shock associated noise and screech tones. *Journal of Sound and Vibration*, 110(2):309–321, October 1986.

[27] Andrey N. Tikhonov and Vasiliy Y. Arsenin. Solutions of ill-posed problems. Translation editor Fritz John. Scripta Series in Mathematics. New York etc.: John Wiley & Sons; Washington, D.C.: V. H. Winston & Sons. XIII, 258 p. (1977)., 1977.